Journal of Power Sources 464 (2020) 228182

Contents lists available at ScienceDirect

Journal of Power Sources

journal homepage: www.elsevier.com/locate/jpowsour

Highly conductive and nonflammable composite polymer electrolytes for rechargeable quasi-solid-state Li-metal batteries

Ziyang Dai [a,1], Jing Yu [b,1], Jiapeng Liu [b], Rong Liu [a], Qi Sun [a], Dengjie Chen [a,**], Francesco Ciucci [b,c,*]

[a] Department of Chemistry, College of Chemistry and Materials Science, Jinan University, Guangzhou, 510632, China
[b] Department of Mechanical and Aerospace Engineering, The Hong Kong University of Science and Technology, Hong Kong, China
[c] Department of Chemical and Biological Engineering, The Hong Kong University of Science and Technology, Hong Kong, China

HIGHLIGHTS

- A highly conductive and nonflammable CPE was developed.
- CPE mainly contains LSTHF, PVDF, and a flame-retarding solvent.
- CPE exhibits conductivities as high as 0.53 and 0.36 mS cm^{-1} at RT and 0 °C.
- The Li/$LiFePO_4$ batteries deliver stable cycling performance between 5 and 60 °C.

GRAPHICAL ABSTRACT

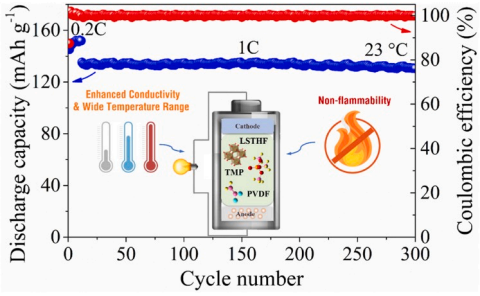

ARTICLE INFO

Keywords:
Solid-state battery
Perovskite Li conductor
Ionic conductivity
Nonflammable composite polymer membrane

ABSTRACT

Solid-state Li-metal batteries are promising as next-generation energy storage devices. However, the main bottlenecks are the poor conductivity of the solid electrolyte and the high interfacial resistance. While polymers exhibit a lower interfacial resistance in comparison to ceramics, they often require the inclusion of flammable solvents. In this work, highly conductive composite polymer electrolyte (CPE) membranes are prepared by integrating a poly(vinylidene fluoride) matrix (PVDF) with a Li-conductive perovskite (i.e., $Li_{0.38}Sr_{0.44}Ta_{0.70}Hf_{0.30}O_{2.95}F_{0.05}$, LSTHF), a flame-retarding solvent (i.e., trimethyl phosphate (TMP)), and a Li salt (i.e., $LiClO_4$). The CPE membrane with 10 wt% LSTHF (CPE-10) exhibits conductivities as high as 0.53 mS cm^{-1} at room temperature (RT) and 0.36 mS cm^{-1} at 0 °C. Furthermore, prototype batteries, including the CPE-10 electrolyte, show high initial discharge capacities, good rate capabilities, and stable cycling performance at either RT or 5 and 60 °C. This study illustrates that including a Li-conductive perovskite and TMP in a PVDF-based polymer material could yield safe, high-performance quasi-solid-state Li-metal batteries capable of operating over a relatively wide temperature range.

* Corresponding author. Department of Mechanical and Aerospace Engineering, The Hong Kong University of Science and Technology, Hong Kong, China.
** Corresponding author.
E-mail addresses: dengjie.chen@jnu.edu.cn (D. Chen), *francesco.ciucci@ust.hk* (F. Ciucci).
[1] These authors contributed equally to this work.

https://doi.org/10.1016/j.jpowsour.2020.228182
Received 6 February 2020; Received in revised form 1 April 2020; Accepted 11 April 2020
Available online 29 April 2020

1. Introduction

Commercial Li-ion batteries (LIBs) are characterized by high energy density, low self-discharge rate, and long cycle life. For those reasons, they play a dominant role in consumer electronics, medical devices, and electric vehicles [1–5]. However, improving the LIBs' energy density and safety is still a significant challenge. Scientific research effort has been devoted to the development of the Li-metal batteries because the Li metal negative electrode has a theoretical specific capacity of 3860 mAh g^{-1}, a value much higher than that of commercial graphite (i.e. 372 mAh g^{-1}) [6–8]. In addition, conventional LIBs always feature organic liquid electrolytes, which are highly flammable [9–11]. Such a safety issue may be overcome by incorporating flame retardants or by developing solid-state electrolytes [12,13]. Highly conductive, nonflammable, and electrochemically stable inorganic/ceramic solid-state electrolytes (SSEs) such as perovskites, garnets, and Li superionic conductors (LISICONs) have been intensively studied [7,14]. However, batteries using ceramic electrolytes always exhibit large interfacial resistances. Furthermore, ceramics are generally brittle and challenging to fabricate [14,15]. In contrast, solid polymer electrolytes (SPEs) such as poly (ethylene oxide) (PEO) and poly(vinylidene fluoride) (PVDF) are easier to process and are flexible [16–18]. However, pure SPEs are still not used in practical applications because of their low ionic conductivity, typically $<10^{-5}$ S cm^{-1}, at room temperature (RT) [13,19,20].

Composite polymer electrolytes (CPEs), which feature inorganic SSE particles in an SPE matrix, leverage the merits of both types of electrolytes [19–21]. Recent studies have demonstrated that the ionic conductivity can be improved by 1) combining SSE fillers into a SPE matrix; 2) introducing the Lewis acid-base interaction between fillers and the Li salts; and 3) forming amorphous polymer phases, which facilitate the dissociation of the Li salt and provide fast-channels for the Li-ion transfer [22–25]. For example, our previous work reported a CPE consisting of $Li_{6.4}La_3Zr_{1.4}Ta_{0.6}O_{12}$ (LLZTO), PVDF, and $LiClO_4$ [26]. The resulting CPE had a relatively high ionic conductivity of 1.1×10^{-4} S cm^{-1}, good tensile strength, and flexibility. It is anticipated that the ionic conductivity of CPEs can be further improved by optimizing the filler materials. Also, although the development of nonflammable electrolytes is of great practical interest, employing nonflammable additives often leads to the deterioration of the electrochemical performance [27]. In a recent article, we introduced a flame-retardant, i.e., trimethyl phosphate (TMP), into a CPE to enhance the nonflammability, without compromising the electrochemical performance [28]. Therefore, simultaneously introducing a high-conductive filler and replacing traditional solvents with flame-retarding TMP could be a practical strategy for developing highly conductive and nonflammable CPEs.

In this work, we synthesized $Li_{0.38}Sr_{0.44}Ta_{0.7}Hf_{0.3}O_{2.95}F_{0.05}$ (LSTHF), a perovskite Li-conductor, with a Li-ion conductivity of 2.2×10^{-4} S cm^{-1} at 23 °C. Then, we applied LSTHF in a CPE, including PVDF, TMP, and $LiClO_4$. The optimized CPE membrane with 10 wt% of LSTHF (CPE-10) was characterized by ionic conductivities as high as 3.6×10^{-4}, 5.3×10^{-4}, and 8.9×10^{-4} S cm^{-1} at 0, 23, and 70 °C, respectively. In addition, the CPE was nonflammable and showed high electrochemical stability until ~4.8 V. Furthermore, batteries with Li as the anode, $LiFePO_4$ (LFP) as the cathode, and CPE-10 as the electrolyte displayed high discharge capacities, excellent rate capabilities, and stable cycling performance with negligible capacity loss when operated over a relatively wide temperature range (i.e. from 5 to 60 °C).

2. Experimental section

2.1. Materials synthesis and preparation of CPEs

LSTHF was synthesized using a solid-state reaction. First, a stoichiometric mixture of Li_2CO_3 (99.9%, MACKLIN), $SrCO_3$ (AR, Sinopharm), Ta_2O_5 (99.5%, Aladdin), HfO_2 (99.9%, Aladdin), and LiF (99.99%, MERYER) was weighed and mixed with ethanol. After ball-milling at 500 rpm for 2 h, the mixed slurry was dried at 200 °C for 2 h and then heated at 900 °C for 12 h in an alumina crucible. An extra 10 wt% of Li_2CO_3 was later added to compensate for the evaporation of the Li. After that, the powder underwent a second ball-milling step in ethanol at 500 rpm for 2 h. This step was followed by drying at 200 °C for 2 h. Subsequently, 0.5 g of the dried powder was uniaxially pressed at 25.0 MPa into a pellet. The resulting disks were then supported and covered by the mother powder to prevent undesirable reactions with alumina. Dense LSTHF pellets were obtained by annealing at 1300 °C for 12 h. Finally, the sintered LSTHF pellets were ground into powder.

The CPE membranes were prepared by a film casting method. First, $LiClO_4$ (99.99%, Sigma-Aldrich) and PVDF (Kynar HSV900, Arkema) were dried in a vacuum oven at 80 °C for 24 h to remove residual moisture. Then, 0.15 g of $LiClO_4$ and 0.45 g of PVDF were mixed with 6.0 mL of TMP (Shanghai Zhanyun Chemical Co, Ltd., 98%). A transparent solution was obtained, which was continually stirred at 50 °C on a hot plate. After that, the LSTHF powder was added to the solution and stirred for 10 h at 60 °C to form a viscous and homogeneous mixture. Note that 0, 10, 20, 30, and 40 wt% relative to the total amount of PVDF and LSTHF were selected. Finally, the obtained mixture was cast onto a glass plate and dried in a vacuum oven at 60 °C for 6 h. The obtained CPEs had a thickness of 130–150 μm. The notation CPE-X (X = 0, 10, 20, 30, and 40) indicates a CPE with X wt% of the LSTHF filler relative to the total amount of PVDF and LSTHF.

Commercial LFP (Aleees, Taiwan) was used as the active cathode material. The cathode was prepared by mixing LFP, PVDF in N-methyl-2-pyrrolidone (NMP, MTI, 99.9%), and Super-P carbon black (MTI, TIMICAL SUPER C65) with a weight ratio of 8: 1: 1. Subsequently, the mixture was cast on an Al foil and dried at 105 °C for 8 h. The mass loading of LFP in the cathode was controlled between 2.0 and 2.5 mg cm^{-2}. The Li metal was used as the anode. Its surface was wet with 2.0 μL of fluoroethylene carbonate (FEC). This process was followed by drying the FEC-coated Li metal at RT for 0.5 h in a glovebox (Mikrouna, $[O_2] < 0.1$ ppm, $[H_2O] < 0.1$ ppm) filled with ultrapure Ar (99.999%, Air products).

2.2. Material characterizations

X-ray diffraction (XRD) patterns were obtained using a PANalytical X'Pert Pro diffractometer with Cu Kα (λ = 1.5406 Å) radiation. Fourier transform infrared (FTIR) spectra were recorded using a VERTEX 70 system. X-ray photoelectron spectra (XPS) were acquired employing a PHI5600 X-ray photoelectron spectrometer with a monochromatic Al X-ray source. The morphology and elemental composition of the materials were determined using a scanning electron microscope (SEM, JEM 6700F) equipped with energy-dispersive X-ray spectroscopy (EDX). The local structure and morphology were analyzed by a high-resolution transmission electron microscope (HRTEM, JEM 2010F). Thermogravimetric analysis (TGA, Q5000-TA) was carried out at a heating rate of 10 °C min^{-1} in flowing N_2 (99.996%, Air Products).

2.3. Electrochemical characterizations

The impedance of the LSTHF pellet and CPEs were measured in Au|LSTHF|Au and SS|CPE-X|SS configurations (SS = stainless steel), respectively. The impedance characterization was recorded by electrochemical impedance spectroscopy (EIS) using an electrochemical workstation (VSP-300, Bio-Logic). EIS was carried out over a frequency range from 1 Hz to 7 MHz with a 10 mV AC signal. The corresponding ionic conductivity (σ) was calculated according to the equation $\sigma = l/RA$, where l is the thickness of the LSTHF or CPE membrane, R is the measured resistance, and A is the nominal contact area between LSTHF and Au or between CPE and SS. The activation energy, E_a, of the CPE membranes was obtained using the Arrhenius equation $\sigma(T) = A\, e^{\frac{-E_a}{RT}}$, where A is a pre-exponential factor, and T is the absolute temperature.

Cyclic voltammetry (CV) was conducted on the FEC-coated Li|CPE-10|SS cell between −1.0 and 5.0 V vs. Li/Li^+ at a scan rate of 5 mV s^{-1}. The CV was used to evaluate the electrochemical window of the CPE membrane. The electrochemical properties (e.g. charge/discharge capacities and cycling performance) of the CPE-based batteries in the FEC coated Li|CPE-10|LFP (CR2032) configuration were studied in the voltage range from 2.5 to 4.2 V at 5, 23 and 60 °C, respectively. For these measurements, a battery testing system (CT2001A, LANHE) was employed. All CR2032 coin cells were assembled inside a glovebox filled with ultrapure Ar (99.999%, Air products).

2.4. Density functional theory (DFT) calculation

The ground-state structure of LSTHF was determined following a similar procedure as our previous work [29,30] and that of others [31,32]. We first enumerated all possible arrangement of cations and anions in a 2 × 2 × 4 supercell [33], which corresponds to the composition $Li_5Sr_7Hf_4Ta_{12}O_{47}F$. 50 structures with the lowest electrostatic energy were used to obtain the ground state of LSHTF by DFT relaxation. All the spin-polarized first-principle calculations were conducted using the Vienna ab *initio* simulation package (VASP) [34,35] with a plane-wave

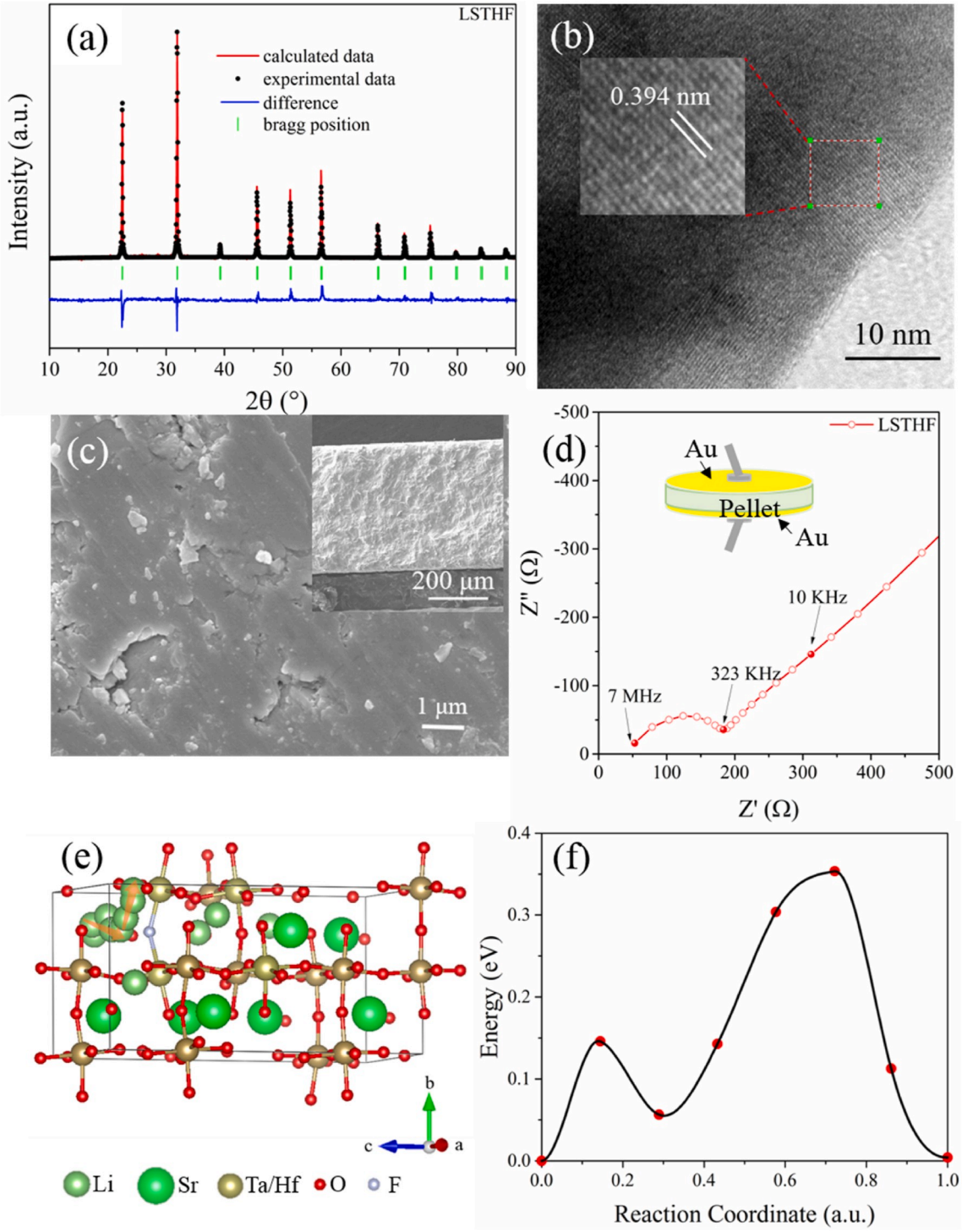

Fig. 1. (a) Rietveld-refined XRD pattern of LSTHF. (b) A HRTEM micrograph of LSTHF. (c) Top and cross-sectional (inset) views of the LSTHF pellet obtained by SEM. (d) A typical Nyquist plot of the EIS measured with a Au|LSTHF|Au cell. (e) The NEB transport path and (f) corresponding energy barrier.

basis set and a projector-augmented wave (PAW) approach [36]. The exchange-correlation was described using the Perdew-Burke-Ernzerhof (PBE) functional [37] under the generalized gradient approximation (GGA) scheme. The kinetic energy cutoff was set as 520 eV. All the structures were allowed to relax using the conjugate gradient method until a convergence of 10^{-5} eV for the energy and 0.02 eV/Å for the force were reached. The first Brillouin zone was sampled with a Γ centered 4 × 4 × 2 k points. To assess the Li-ion defect transport barriers, we carried out climbing image nudged elastic band (CINEB) calculations [38] with 6 images.

3. Results and discussion

3.1. Chemical and physical properties of LSTHF

The basic properties of the LSTHF pellet were investigated before the preparation of CPEs. First, the corresponding phase structure was determined by XRD, as shown in Fig. 1a. A typical XRD pattern indicated that LSTHF had a cubic $Pm\bar{3}m$ structure with the calculated lattice parameter of a = b = c = 3.997 Å. Rietveld refinement results matched well with that of $KTaO_3$ (ICDD 00-038-1470) and those obtained in recent studies on similar perovskite electrolytes [39,40]. Lattice fringes in the HRTEM image indicated a lattice spacing of 3.94 Å for the (001) lattice planes (Fig. 1b), consistent with the XRD pattern. Fig. 1c shows the top and cross-sectional SEM views of the dense LSTHF pellet. The EDS maps of LSTHF suggested that the Sr, Ta, Hf, and F were uniformly distributed (Fig. S1). The EIS of a dense LSTHF pellet measured at 23 °C is shown in Fig. 1d. Therefore, the resulting total ionic conductivity was estimated to be 2.2 × 10^{-4} S cm^{-1} at 23 °C. As expected, the obtained conductivity of LSTHF is higher than that of typical perovskite $Li_{0.34}La_{0.51}TiO_{2.94}$ (7 × 10^{-5} S cm^{-1} at room temperature) [41], and similar to that reported by the Goodenough group [39,40]. In addition to its relatively high ionic conductivity, LSTHF also benefits from chemical stability against moisture [40]. To understand the origin of the high Li-ion conductivity of LSTHF, we performed CINEB calculations. According to the CINEB transport path (Fig. 1e), the hopping barrier of Li-ion was around 0.35 eV (Fig. 1f), which is comparable to other computationally reported solid-state electrolytes such as $Li_{1+x}Ta_{1-x}Zr_xSiO_5$ [42] and $Li_{7-3x}Ga_xLa_3Zr_2O_{12}$, x = 0.1, 0.15 [43]. The obtained LSTHF pellet was ground into powder with an average particle diameter of below 5 μm (Fig. S2).

3.2. LSTHF content-dependent conductivity and mechanical properties of CPEs

CPEs with different contents of LSTHF (from 0 to 40 wt%) were prepared to systematically investigate the conductivity and mechanical properties of CPEs. The EIS of the CPE-X (X = 0, 10, 20, 30, and 40) were obtained with a SS|CPE-X|SS configuration (Fig. S3). The experiments were conducted at 0, 23, 50, and 70 °C. For all investigated temperatures, CPE-10 showed the highest conductivity. Fig. 2a plots the ionic conductivities varied with the LSTHF loading and cell temperature. Specifically, the conductivities of CPE-10 were calculated to be ~3.6 × 10^{-4} S cm^{-1} at 0 °C, ~5.3 × 10^{-4} S cm^{-1} at 23 °C, ~6.8 × 10^{-4} S cm^{-1} at 50 °C and ~8.9 × 10^{-4} S cm^{-1} at 70 °C. The obtained conductivities are higher or comparable to those of other CPEs reported in the literature such as poly(ethylene oxide) (PEO)/LLZTO [44], polyacrylonitrile/$Li_{0.33}La_{0.557}TiO_3$ [45], and PVDF/LLZTO [20]. The absence of a large interfacial resistance and the achievement of high ionic conductivities likely originate from the incorporation of the Li-conductive LSTHF powder, the formation of polar phases in the PVDF matrix, and the inclusion of the Li salt [46,47].

The E_a of CPE-10 was estimated to be 0.126 eV, which was lower than that of CPE-0 (0.136 eV), as shown in the Arrhenius plots in Fig. 2b. With the further addition of LSTHF, the E_a increased possibly because of the aggregation of the LSTHF powder. This aggregation was evidenced by the element distribution from the EDX mapping images of CPEs. As shown in Fig. S4a, $LiClO_4$ (Cl), TMP (P), and PVDF (F) appeared to be uniformly distributed in CPE-0. LSTHF (Ta) was also evenly distributed in CPE-10 and CPE-20, as shown in Figs. S4b and c. However, the LSTHF powder did not disperse well for CPE-30 and CPE-40 (Figs. S4d and e), suggesting particle aggregation. Overall, the CPEs exhibited a similar E_a as that of other liquid electrolytes (e.g. 0.18 eV of ether-based liquid electrolyte) [47].

The impact of the LSTHF filler on the mechanical properties of CPEs was also investigated since the mechanical strength of CPEs is critical for applications [48]. It has been reported that to suppress the growth of Li dendrites, both high stress and high strain are essential in polymer-based electrolytes [48]. As shown in Fig. 2c, the stress and strain response of CPE-10 greatly improved relative to CPE-0, suggesting that the LSTHF filler with a homogeneous distribution contributed to improving the mechanical strength. Although the stress gradually increased with the further addition of the LSTHF filler, the strain decreased rapidly due to the introduction of the secondary phase in the polymer. In light of the above-mentioned performance, the following will solely focus on the CPE-10 material.

3.3. Structure, flexibility, morphology and thermal stability of CPE-10

In this section, the basic properties of the components and the corresponding CPE-10 membrane are illustrated. Fig. 3a shows typical XRD patterns of CPE-10, PVDF, and LSTHF. As observed, LSTHF preserved its structure without peak broadening or shifting after compositing with other components. In contrast, the phase evolution of PVDF was evidenced by the disappearance of three distinct peaks at ~18.4°, ~20.0°, and 26.6° of the pristine PVDF, and the appearance of a broad peak at ~20.2° in CPE-10. These results suggested that PVDF in the membrane changed from a nonpolar structure (i.e. α phase) to a mixture of polar β/γ phases, in line with previous reports on PVDF-based CPEs [26,49]. In addition to the XRD results, Raman spectra suggested the structural evolution of the PVDF matrix after the formation of CPE-10 (Fig. 3b). The peak at 2980 cm^{-1} was no longer distinct for the CPE-10 membrane,

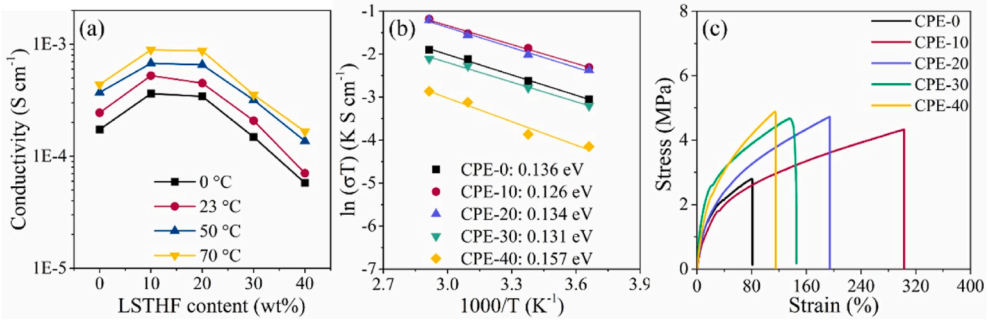

Fig. 2. (a) Content and temperature-dependent conductivity, (b) Arrhenius plots, and (c) stress-strain curves of the CPEs.

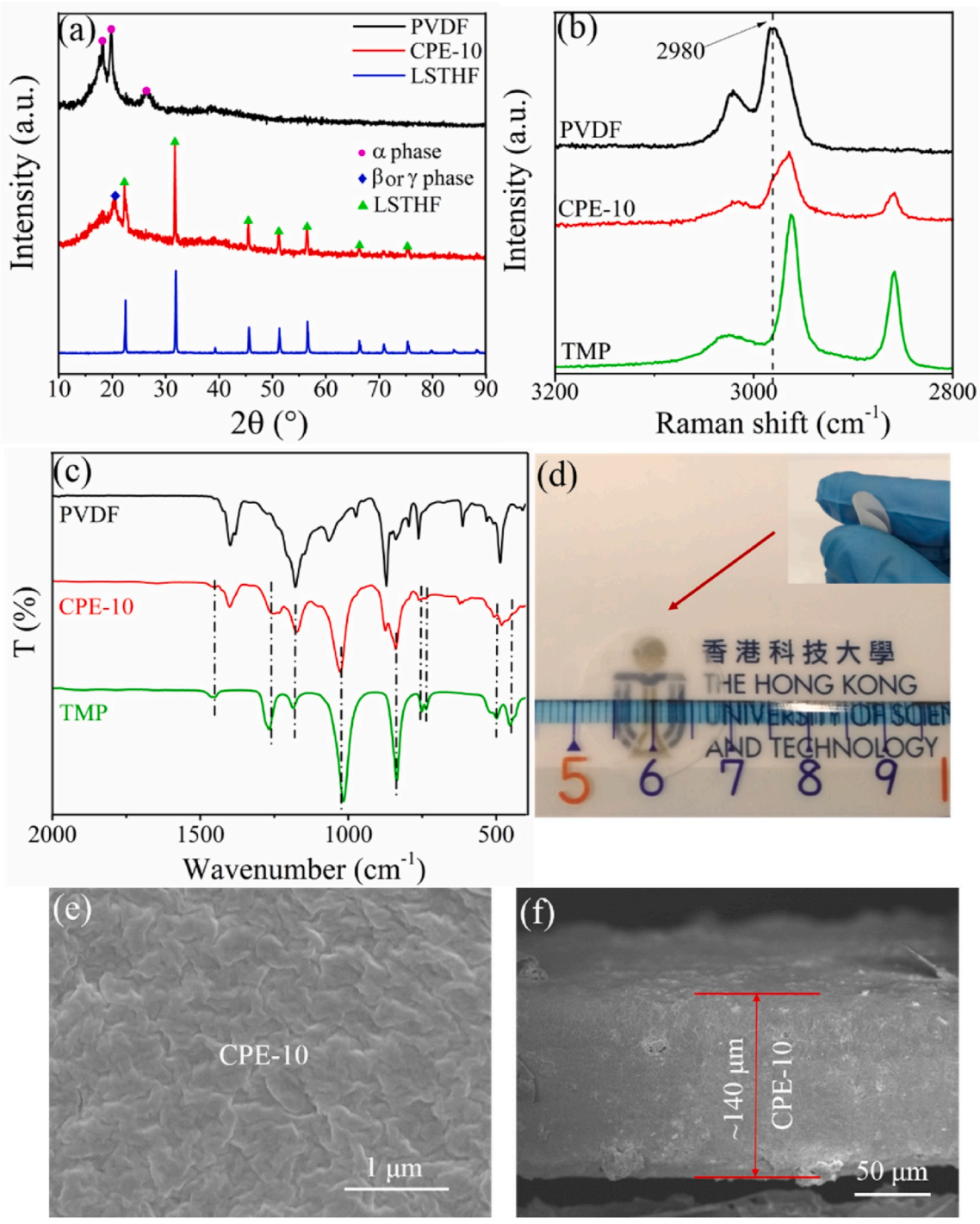

Fig. 3. (a) XRD patterns of PVDF, CPE-10, and LSTHF powder. (b) Raman spectra of TMP, PVDF, and CPE-10. (c) FTIR of PVDF, CPE-10, and TMP. (d) Digital photographs of CPE-10 showing transparent and bendable properties. (e) Top and (f) cross-sectional views of CPE-10 observed by SEM.

while this peak was evident in the pure PVDF. This change indicated deprotonation of CH_2 [50], since the peak belonged to the CH_2 bending vibration mode. Regarding the TMP solvent, the presence of characteristic FTIR peaks of TMP in CPE-10 (Fig. 3c) demonstrated the incorporation and preservation of TMP after the formation of the CPE membrane.

Fig. 3d presents digital photographs of the free-standing CPE membrane, which is flexible, bendable, and transparent. Top and cross-sectional views of SEM images of CPE-10 are shown in Fig. 3e and f. It is worth noting that the thickness of a typical CPE-10 membrane was ~140 μm. Moreover, it was observed that CPE-10 was flame-retardant since it did not catch fire in a flame, see Video S1.

Supplementary video related to this article can be found at https://doi.org/10.1016/j.jpowsour.2020.228182.

The thermal stability of PVDF and CPE-10 was evaluated by TGA, which was conducted from room temperature to 600 °C (Fig. S5). The pure PVDF powder decomposed at ~429 °C, consistent with the literature [26]. As expected, the thermal stability of CPE-10 decreased due to the introduction of secondary phases such as TMP, $LiClO_4$, and LSTHF. The weight loss before 100 °C was due to the adsorbed moisture.

The weight loss observed from 100 to 347 °C for CPE-10 can be ascribed to the combination of several factors, including the evaporation

of the free TMP and TMP present within the membrane, and the degradation induced by scission of the polymer chain. Furthermore, the weight loss that started at ~365 °C and ~450 °C might be due to the decomposition of $LiClO_4$ and the PVDF matrix, respectively.

3.4. Basic electrochemical properties

The Li^+ transference number (t_{Li^+}), a critical factor for Li batteries [8], was obtained from chronoamperometry and EIS of cells in a symmetric Li/Li configuration. The value of t_{Li^+} was computed using [51].

$$t_{Li^+} = \frac{I_{ss}(\Delta V - I_0 R_0)}{I_0(\Delta V - I_{ss} R_{ss})} \quad (1)$$

where I_0 and I_{ss} are the initial and steady-state currents, and R_0 and R_{ss} are the initial and steady-state resistances. Further, the applied DC potential difference (ΔV) was set at 10 mV. The measured chronoamperometry and EIS tests are reported in Fig. S6. The R_0 and R_{ss} were obtained from EIS using a common equivalent circuit consisting of two ZARCs in series. The t_{Li^+} estimated for CPE-0 and CPE-10 were calculated to be ~0.46 and ~0.50, respectively. The slightly large transference number of CPE-10 in comparison to that of CPE-0 may result from the introduction of the LSTHF filler. One should note that these relatively high t_{Li^+} values are within the literature range of 0.3–0.6 [52,53].

Generally, perovskites with easily reducible cations are unstable against the metallic Li [39], and polymers are electrochemically unstable at high potentials vs. Li/Li^+ [54]. To evaluate the electrochemical stability of CPE-10 against the Li metal anode and to determine the electrochemical window, CV was carried out in the voltage range between −1.0 and 5.0 V vs. Li/Li^+ at a scan rate of 5 mV s^{-1} at 23 °C. As shown in Fig. S7, CPE-10 exhibited an oxidative current of 0.03 mA at ~3.6 V vs. Li/Li^+ for the bare Li|CPE-10|SS cell. Therefore, the addition of LSTHF showed a limited contribution to the increase of the electrochemical window voltage. This observation is different from previous reports that adding fillers generally benefits the electrochemical stability window [22,55]. Our results suggest that the oxidation potential also depends on the reducibility of the filler. Unfortunately, when in contact with Li metal, Ta^{5+} in LSTHF (Fig. S8a) was reduced easily, as evidenced by the appearance of the Ta^0 peak (Fig. S8b). In this context, to form a LiF-rich SEI layer and to suppress the reduction of LSTHF (Ta^{5+}), the Li-metal anode was coated with FEC. This method has been demonstrated to be effective in enhancing the stability window [28]. Consequently, even at a potential as high as 4.8 V vs. Li/Li^+, an oxidative current of only ~0.03 mA was observed for the FEC-coated Li|CPE-10|SS cell (Fig. 4a). CV also allowed us to identify two redox peaks between −1.0 and 1.0 V vs. Li/Li^+ that correspond to the Li deposition and dissolution [56]. The peaks of the Li deposition and dissolution differed dramatically, and the peak intensity of the FEC-coated Li|CPE-10|SS cell (Fig. 4a) overwhelmed that of the Li|CPE-10|SS cell and FEC-coated Li|CPE-0|SS (Fig. S7), indicating that both the addition of LSTHF and FEC coating greatly reduced the resistance during Li deposition/dissociation.

To further investigate the compatibility between CPE-10 and the FEC-coated Li metal, a Li plating and stripping experiment was carried out using a Li|CPE-10|Li symmetric cell with a current density of ±0.2 mA cm^{-2} at 23 °C (Fig. 4b). The potential response of the symmetric cell in the initial 220 cycles gradually decreased. Then, CPE-10 operated stably for over 500 h with a response voltage of approximately ±0.14 mV, suggesting excellent electrochemical compatibility between the FEC-coated Li metal and CPE-10. The homogeneous contact between the Li metal and CPE-10 and the formation of a LiF-rich SEI layer resulting from the FEC coating likely accounted for the stable response [28]. Fig. 4c shows the corresponding EIS response before and after cycling. An equivalent circuit in Fig. 4c was used to estimate the charge transfer resistances, whose value was ~1049 Ω in the first cycle, and decreased to ~515 Ω after 500 cycles, suggesting improvement of the interfacial contacts after plating and stripping. The morphology of the Li metal before and after cycling was studied by SEM and displayed no obvious difference (Fig. 4d and e). As shown in Fig. 4e and Fig. S9, no visible mossy Li was found after 500 cycles, indicating a uniform Li deposition/dissociation during the plating/stripping process. This may possibly be due to the good dispersion of LSTHF in the PVDF matrix, as well as the FEC coating that suppressed the growth of Li dendrites [57–59].

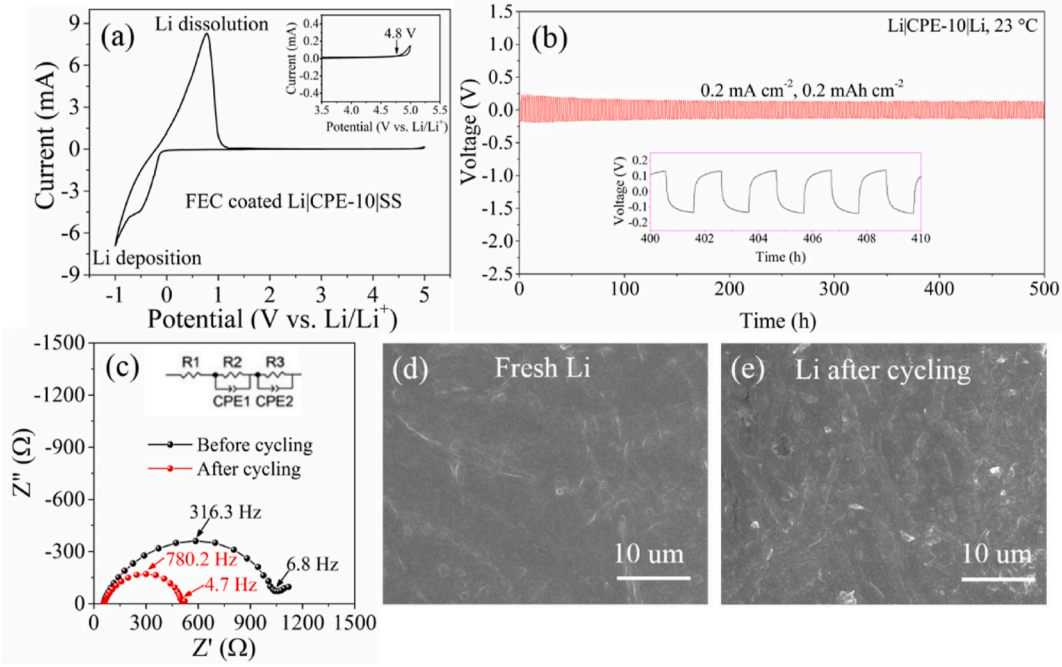

Fig. 4. (a) Cyclic voltammetry of the FEC-coated Li|CPE-10|SS cell. (b) Plating and stripping measurement of the symmetric FEC-coated Li|CPE-10| FEC-coated Li cell. (c) EIS of the symmetric FEC-coated Li|CPE-10| FEC-coated Li cell before and after cycling. SEM images of the surface of the Li anode (d) before and (e) after cycling.

3.5. Cell performance operating at a wide temperature range

The cycling stability and rate performance of the full battery (FEC-coated Li|CPE-10|LFP) were evaluated at a wide temperature range from 5 to 60 °C. At 23 °C, the cell displayed an initial discharge capacity of 146 mAh g^{-1} with an initial Coulombic efficiency (CE) of 85.9% at 0.2C (Fig. 5a). As exhibited in Fig. 5b, the CE increased to 99.8%, and the discharge capacity slightly increased due to the formation of a stable SEI layer. The discharge capacity of 134 mAh g^{-1} was obtained when switching to 1C. Even after 300 cycles, a discharge capacity of 131 mAh g^{-1} and a CE of >99.8% at 1C were preserved, suggesting excellent cycling stability. The cell with CPE-10 also delivered an excellent rate performance, as shown in Fig. 5c and d. Typical discharge capacities of ~153, ~144, ~134, ~122, ~112, ~105, and 98 mAh g^{-1} displayed at 0.2C, 0.5C, 1C, 2C, 3C, 4C, and 5C, respectively (Fig. 5c). When the C-rate went back to 1C, the discharge capacity remained at ~134 mAh g^{-1} and the capacity retention of ~100% maintained for over 150 cycles (Fig. 5d). The corresponding EIS spectra are shown in Fig. S10 and the resistance decreased from 545 Ω to 190 Ω after 150 cycles; such a decrease is attributable to the formation of a stable SEI layer induced by the addition of 2 μL of FEC.

Generally, a relatively narrow operation temperature range near room temperature is recommended for the operation of commercial LIBs employing organic liquid electrolytes since the degradation of electrochemical performance might speed up at elevated temperatures (e.g., 60 °C) due to the promoted side reactions [60]. The degradation might further worsen when applying the highly active lithium metal as the anode. Nevertheless, a recent report demonstrated that a battery with a high CE and cycling stability was realized at 60 °C when adopting the ether-based electrolyte [60], suggesting the replacement of traditional electrolytes could widen the operating temperature range. To evaluate the electrochemical performance of CPE-10 beyond RT, the FEC-coated Li|CPE-10|LFP battery was cycled at 60 °C for further analysis. As shown in Fig. 6a, even after 100 cycles, the battery maintained the discharge capacity of 148.8 mAh g^{-1} at 1C (Fig. 6a & Fig. S11a).

Since the ionic conductivity of CPE-10 is approximately 3.6×10^{-4} S cm^{-1} at 0 °C, the CPE-10-based Li/LFP battery was further tested in an ice bath (~5 °C), delivering a discharge capacity of 118.4 mAh g^{-1} at 1C and capacity retention of 91.8% after 100 cycles (Fig. 6b & Fig. S11b). Table 1 summarizes some recent publications on Li/LFP batteries when operating at different temperatures. The cycling stability and rate performance of the Li/LFP battery with our CPE membrane and configuration exceed most of the previously reported results in the literature [20,60–64].

4. Conclusions

We developed new flexible CPE membranes by combining the Li-conductive perovskite LSTHF, TMP, PVDF, and $LiClO_4$. Typically, CPE-10 showed high ionic conductivities of $\sim 3.6 \times 10^{-4}$ S cm^{-1} at 0 °C, $\sim 5.3 \times 10^{-4}$ S cm^{-1} at 23 °C, $\sim 6.8 \times 10^{-4}$ S cm^{-1} at 50 °C, and $\sim 8.9 \times 10^{-4}$ S cm^{-1} at 70 °C. In addition to benefitting from the presence of PVDF and the Li salt, the conductivity of CPEs increased because highly conductive LSTHF was introduced. The high conductivity of LSTHF originates from the low hopping barrier of Li ions, as shown by the DFT calculations. CPE-10 was also characterized to be nonflammable thanks to the employment of the flame-retardant TMP. Moreover, the integration of CPE-10 with the FEC-coated Li metal suppressed the growth of Li dendrites and the corresponding batteries exhibited excellent electrochemical stability when operating at a wide temperature range of 5 and 60 °C. This work indicates that by simultaneously employing a highly conductive filler and a flame-retardant solvent within PVDF, the quasi-solid-state Li-metal batteries have great potential to satisfy the high energy density and safety requirements.

Declaration of competing interest

The authors declared that they have no conflicts of interest to this work.

CRediT authorship contribution statement

Ziyang Dai: Conceptualization, Investigation. **Jing Yu:** Conceptualization, Methodology, Formal analysis, Investigation, Writing - original draft. **Jiapeng Liu:** Software. **Rong Liu:** Investigation. **Qi Sun:** Investigation. **Dengjie Chen:** Resources, Writing - original draft, Writing - review & editing, Supervision. **Francesco Ciucci:** Resources, Writing - review & editing, Supervision.

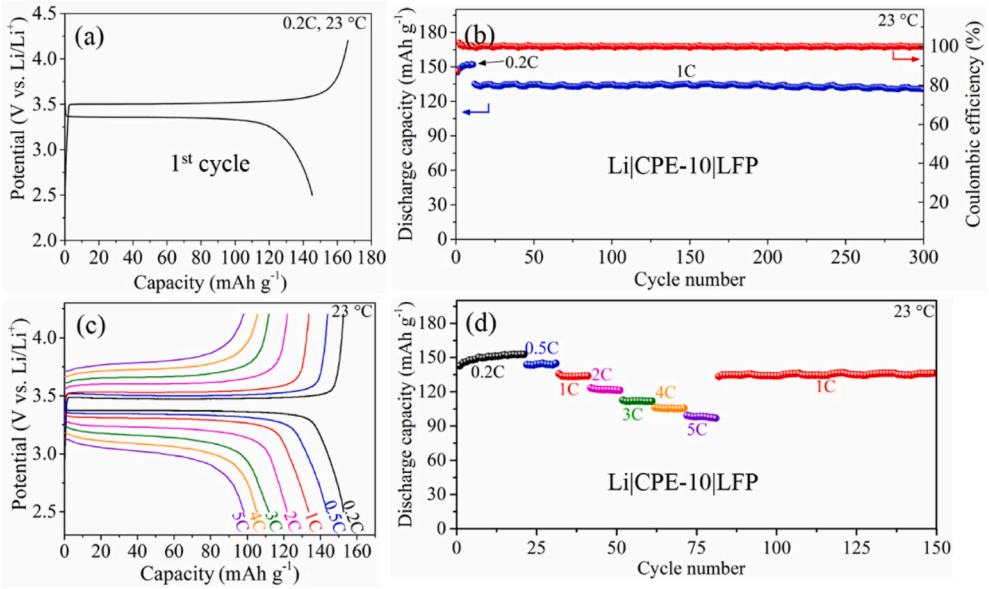

Fig. 5. (a) The first charge/discharge curves of the asymmetrical FEC-coated Li|CPE-10|LFP cell with a 0.2C-rate at 23 °C. (b) Cycling performance of the FEC-coated Li|CPE-10|LFP cell at 0.2C for the initial 10 cycles and 1C for the remaining 290 cycles at 23 °C. (c) Typical charge/discharge curves at various C-rates of the FEC-coated Li|CPE-10|LFP cell at 23 °C. (d) Rate performance of the FEC-coated Li|CPE-10|LFP cell at various C-rates at 23 °C.

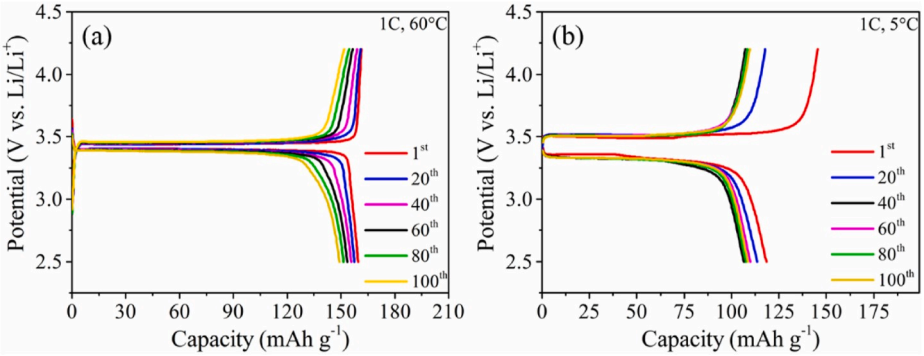

Fig. 6. Typical charge/discharge curves of the FEC-coated Li|CPE-10|LFP batteries operated at (a) 60 °C and (b) 5 °C. Note: Before the measurement at elevated and low temperatures, the FEC-coated Li|CPE-10|LFP batteries cycled at 23 °C for 15 cycles.

Table 1
Comparison of the electrochemical performance of Li/LFP cells with representative electrolytes.

Electrolytes	Operating potential (V)	C-Rate	Discharge capacity (mA h g^{-1})	Operating Temperature (°C)	Ref.
Ether-based electrolyte	2.5–3.75	1C	133	20	[60]
		1C	146	60	
PVDF-based CPE	3.0–4.2	0.4C	150	RT	[20]
Poly(propylene carbonate)/$Li_{6.75}La_3Zr_{1.75}Ta_{0.25}O_{12}$ composite solid electrolyte	2.5–4.0	1C	40	5	[61]
		0.5C	116	20	
		3C	114	120	
Deep eutectic solvent-silica CPE	2.5–4.2	0.1C	112	RT	[62]
Anion-immobilized polymer electrolyte	/	1C	100	10	[63]
		1C	115	30	
		1C	140	60	
3D polymer electrolyte	2.5–4.0	1C	126	25	[64]
LSTHF + PVDF + TMP	2.5–4.2	1C	118	5	**This work**
		1C	134	23	
		1C	149	60	

Acknowledgments

D.C. gratefully acknowledges the National Natural Science Foundation of China (No. 51702125) and the Pearl River S&T Nova Program of Guangzhou (No. 201806010054). J. Y., J. L., and F.C. gratefully acknowledge the Hong Kong Innovation and Technology Fund (No. ITS/292/18FP), the Research Grants Council of Hong Kong for support through the projects (16207615, 16227016, and 16204517), and the Guangzhou Science and Technology Program (No. 201807010074).

Appendix A. Supplementary data

Supplementary data to this article can be found online at https://doi.org/10.1016/j.jpowsour.2020.228182.

References

[1] J.M. Tarascon, M. Armand, Issues and challenges facing rechargeable lithium batteries, Nature 414 (2001) 359–367.
[2] B. Dunn, H. Kamath, J.-M. Tarascon, Electrical energy storage for the grid: a battery of choices, Science 334 (2011) 928.
[3] M. Armand, J.M. Tarascon, Building better batteries, Nature 451 (2008) 652–657.
[4] M.S. Whittingham, Lithium batteries and cathode materials, Chem. Rev. 104 (2004) 4271–4302.
[5] V. Etacheri, R. Marom, R. Elazari, G. Salitra, D. Aurbach, Challenges in the development of advanced Li-ion batteries: a review, Energy Environ. Sci. 4 (2011) 3243–3262.
[6] P. Albertus, S. Babinec, S. Litzelman, A. Newman, Status and challenges in enabling the lithium metal electrode for high-energy and low-cost rechargeable batteries, Nat. Energy 3 (2018) 16–21.
[7] T. Jiang, P. He, G. Wang, Y. Shen, C.-W. Nan, L.-Z. Fan, Solvent-free synthesis of thin, flexible, nonflammable garnet-based composite solid electrolyte for all-solid-state lithium batteries, Adv. Energy Mater. 10 (2020), 1903376.
[8] L. Chen, W. Li, L.-Z. Fan, C.-W. Nan, Q. Zhang, Intercalated electrolyte with high transference number for dendrite-free solid-state lithium batteries, Adv. Funct. Mater. 29 (2019), 1901047.
[9] W. Xu, J. Wang, F. Ding, X. Chen, E. Nasybulin, Y. Zhang, J.-G. Zhang, Lithium metal anodes for rechargeable batteries, Energy Environ. Sci. 7 (2014) 513–537.
[10] J. Wang, Y. Yamada, K. Sodeyama, E. Watanabe, K. Takada, Y. Tateyama, A. Yamada, Fire-extinguishing organic electrolytes for safe batteries, Nat. Energy 3 (2018) 22–29.
[11] J. Wu, J. Liu, Z. Lu, K. Lin, Y.-Q. Lyu, B. Li, F. Ciucci, J.-K. Kim, Non-flammable electrolyte for dendrite-free sodium-sulfur battery, Energy Storage Mater. 23 (2019) 8–16.
[12] Z. Lu, J. Yu, J. Wu, M.B. Effat, S.C.T. Kwok, Y. Lyu, M.M.F. Yuen, F. Ciucci, Enabling room-temperature solid-state lithium-metal batteries with fluoroethylene carbonate-modified plastic crystal interlayers, Energy Storage Mater. 18 (2019) 311–319.
[13] A. Manthiram, X. Yu, S. Wang, Lithium battery chemistries enabled by solid-state electrolytes, Nat. Rev. Mater. 2 (2017), 16103.
[14] V. Thangadurai, S. Narayanan, D. Pinzaru, Garnet-type solid-state fast Li ion conductors for Li batteries: critical review, Chem. Soc. Rev. 43 (2014) 4714–4727.
[15] T. Famprikis, P. Canepa, J.A. Dawson, M.S. Islam, C. Masquelier, Fundamentals of inorganic solid-state electrolytes for batteries, Nat. Mater. 18 (2019) 1278–1291.
[16] W.H. Meyer, Polymer electrolytes for lithium-ion batteries, Adv. Mater. 10 (1998) 439–448.
[17] L. Long, S. Wang, M. Xiao, Y. Meng, Polymer electrolytes for lithium polymer batteries, J. Mater. Chem. 4 (2016) 10038–10069.
[18] S. Muench, A. Wild, C. Friebe, B. Häupler, T. Janoschka, U.S. Schubert, Polymer-based organic batteries, Chem. Rev. 116 (2016) 9438–9484.
[19] F. Croce, G.B. Appetecchi, L. Persi, B. Scrosati, Nanocomposite polymer electrolytes for lithium batteries, Nature 394 (1998) 456–458.
[20] C. Sun, J. Liu, Y. Gong, D.P. Wilkinson, J. Zhang, Recent advances in all-solid-state rechargeable lithium batteries, Nano Energy 33 (2017) 363–386.
[21] J. Hu, P. He, B. Zhang, B. Wang, L.-Z. Fan, Porous film host-derived 3D composite polymer electrolyte for high-voltage solid state lithium batteries, Energy Storage Mater. 26 (2020) 283–289.
[22] Y. Shi, D. Tan, M. Li, Z. Chen, Nanohybrid electrolytes for high-energy lithium-ion batteries: recent advances and future challenges, Nanotechnology 30 (2019), 302002.
[23] R. Tan, R. Gao, Y. Zhao, M. Zhang, J. Xu, J. Yang, F. Pan, Novel organic–inorganic hybrid electrolyte to enable LiFePO4 quasi-solid-state Li-ion batteries performed

highly around room temperature, ACS Appl. Mater. Interfaces 8 (2016) 31273–31280.
[24] W. Liu, D. Lin, J. Sun, G. Zhou, Y. Cui, Improved lithium ionic conductivity in composite polymer electrolytes with oxide-ion conducting nanowires, ACS Nano 10 (2016) 11407–11413.
[25] X. Zhang, T. Liu, S. Zhang, X. Huang, B. Xu, Y. Lin, B. Xu, L. Li, C.-W. Nan, Y. Shen, Synergistic coupling between $Li_{6.75}La_3Zr_{1.75}Ta_{0.25}O_{12}$ and poly(vinylidene fluoride) induces high ionic conductivity, mechanical strength, and thermal stability of solid composite electrolytes, J. Am. Chem. Soc. 139 (2017) 13779–13785.
[26] J. Yu, S.C.T. Kwok, Z. Lu, M.B. Effat, Y.-Q. Lyu, M.M.F. Yuen, F. Ciucci, A ceramic-pvdf composite membrane with modified interfaces as an ion-conducting electrolyte for solid-state lithium-ion batteries operating at room temperature, ChemElectroChem 5 (2018) 2873–2881.
[27] H.F. Xiang, H.Y. Xu, Z.Z. Wang, C.H. Chen, Dimethyl methylphosphonate (DMMP) as an efficient flame retardant additive for the lithium-ion battery electrolytes, J. Power Sources 173 (2007) 562–564.
[28] J. Yu, Y.-Q. Lyu, J. Liu, M.B. Effat, S.C.T. Kwok, J. Wu, F. Ciucci, Enabling non-flammable Li-metal batteries via electrolyte functionalization and interface engineering, J. Mater. Chem. 7 (2019) 17995–18002.
[29] J. Liu, Z. Lu, M.B. Effat, F. Ciucci, A theoretical study on the stability and ionic conductivity of the $Na_{11}M_2PS_{12}$ (M=Sn, Ge) superionic conductors, J. Power Sources 409 (2019) 94–101.
[30] Z. Lu, F. Ciucci, Anti-perovskite cathodes for lithium batteries, J. Mater. Chem. 6 (2018) 5185–5192.
[31] S.P. Ong, Y. Mo, W.D. Richards, L. Miara, H.S. Lee, G. Ceder, Phase stability, electrochemical stability and ionic conductivity of the $Li_{10\pm1}MP_2X_{12}$ (M = Ge, Si, Sn, Al or P, and X = O, S or Se) family of superionic conductors, Energy Environ. Sci. 6 (2013) 148–156.
[32] Z. Deng, Z. Zhu, I.-H. Chu, S.P. Ong, Data-driven first-principles methods for the study and design of alkali superionic conductors, Chem. Mater. 29 (2017) 281–288.
[33] K. Okhotnikov, T. Charpentier, S. Cadars, Supercell Program: a combinatorial structure-generation approach for the local-level modeling of atomic substitutions and partial occupancies in crystals, J. Cheminf. 8 (2016) 17.
[34] G. Kresse, J. Furthmüller, Efficient iterative schemes for ab initio total-energy calculations using a plane-wave basis set, Phys. Rev. B 54 (1996), 11169.
[35] G. Kresse, J. Furthmüller, Efficiency of ab-initio total energy calculations for metals and semiconductors using a plane-wave basis set, Comput. Mater. Sci. 6 (1996) 15–50.
[36] P.E. Blöchl, Projector augmented-wave method, Phys. Rev. B 50 (1994), 17953.
[37] J.P. Perdew, K. Burke, M. Ernzerhof, Generalized gradient approximation made simple, Phys. Rev. Lett. 77 (1996) 3865–3868.
[38] G. Henkelman, B.P. Uberuaga, H. Jónsson, A climbing image nudged elastic band method for finding saddle points and minimum energy paths, J. Chem. Phys. 113 (2000) 9901–9904.
[39] B. Huang, B. Xu, Y. Li, W. Zhou, Y. You, S. Zhong, C.-A. Wang, J.B. Goodenough, Li-ion conduction and stability of perovskite $Li_{3/8}Sr_{7/16}Hf_{1/4}Ta_{3/4}O_3$, ACS Appl. Mater. Interfaces 8 (2016) 14552–14557.
[40] Y. Li, H. Xu, P.-H. Chien, N. Wu, S. Xin, L. Xue, K. Park, Y.-Y. Hu, J.B. Goodenough, A perovskite electrolyte that is stable in moist Air for lithium-ion batteries, Angew. Chem. Int. Ed. 57 (2018) 8587–8591.
[41] Y. Inaguma, C. Liquan, M. Itoh, T. Nakamura, T. Uchida, H. Ikuta, M. Wakihara, High ionic conductivity in lithium lanthanum titanate, Solid State Commun. 86 (1993) 689–693.
[42] S. Xiong, X. He, A. Han, Z. Liu, Z. Ren, B. McElhenny, A.M. Nolan, S. Chen, Y. Mo, H. Chen, Computation-guided design of $LiTaSiO_5$, a new lithium ionic conductor with sphene structure, Adv. Energy Mater. 9 (2019), 1803821.
[43] J.-F. Wu, E.-Y. Chen, Y. Yu, L. Liu, Y. Wu, W.K. Pang, V.K. Peterson, X. Guo, Gallium-doped $Li_7La_3Zr_2O_{12}$ garnet-type electrolytes with high lithium-ion conductivity, ACS Appl. Mater. Interfaces 9 (2017) 1542–1552.
[44] J. Zhang, N. Zhao, M. Zhang, Y. Li, P.K. Chu, X. Guo, Z. Di, X. Wang, H. Li, Flexible and ion-conducting membrane electrolytes for solid-state lithium batteries: dispersion of garnet nanoparticles in insulating polyethylene oxide, Nano Energy 28 (2016) 447–454.
[45] W. Liu, N. Liu, J. Sun, P.-C. Hsu, Y. Li, H.-W. Lee, Y. Cui, Ionic conductivity enhancement of polymer electrolytes with ceramic nanowire fillers, Nano Lett. 15 (2015) 2740–2745.
[46] Y.J. Lim, H.W. Kim, S.S. Lee, H.J. Kim, J.-K. Kim, Y.-G. Jung, Y. Kim, Ceramic-based composite solid electrolyte for lithium-ion batteries, ChemPlusChem 80 (2015) 1100–1103.
[47] J.-K. Kim, Y.J. Lim, H. Kim, G.-B. Cho, Y. Kim, A hybrid solid electrolyte for flexible solid-state sodium batteries, Energy Environ. Sci. 8 (2015) 3589–3596.
[48] T. Dong, J. Zhang, G. Xu, J. Chai, H. Du, L. Wang, H. Wen, X. Zang, A. Du, Q. Jia, A multifunctional polymer electrolyte enables ultra-long cycle-life in a high-voltage lithium metal battery, Energy Environ. Sci. 11 (2018) 1197–1203.
[49] S.K. Karan, R. Bera, S. Paria, A.K. Das, S. Maiti, A. Maitra, B.B. Khatua, An approach to design highly durable piezoelectric nanogenerator based on self-poled PVDF/AlO-rGO flexible nanocomposite with high power density and energy conversion efficiency, Adv. Energy Mater. 6 (2016), 1601016.
[50] S. Zhang, J. Shen, X. Qiu, D. Weng, W. Zhu, Esr and vibrational spectroscopy study on poly(vinylidene fluoride) membranes with alkaline treatment, J. Power Sources 153 (2006) 234–238.
[51] J. Evans, C.A. Vincent, P.G. Bruce, Electrochemical measurement of transference numbers in polymer electrolytes, Polymer 28 (1987) 2324–2328.
[52] P.G. Bruce, J. Evans, C.A. Vincent, Conductivity and transference number measurements on polymer electrolytes, Solid State Ionics 28–30 (1988) 918–922.
[53] A. Manuel Stephan, K.S. Nahm, Review on composite polymer electrolytes for lithium batteries, Polymer 47 (2006) 5952–5964.
[54] S. Choudhury, Z. Tu, A. Nijamudheen, M.J. Zachman, S. Stalin, Y. Deng, Q. Zhao, D. Vu, L.F. Kourkoutis, J.L. Mendoza-Cortes, L.A. Archer, Stabilizing polymer electrolytes in high-voltage lithium batteries, Nat. Commun. 10 (2019) 3091.
[55] W. Li, S. Zhang, B. Wang, S. Gu, D. Xu, J. Wang, C. Chen, Z. Wen, Nanoporous adsorption effect on alteration of the Li^+ diffusion pathway by a highly ordered porous electrolyte additive for high-rate all-solid-state lithium metal batteries, ACS Appl. Mater. Interfaces 10 (2018) 23874–23882.
[56] Y. Li, W. Zhou, X. Chen, X. Lü, Z. Cui, S. Xin, L. Xue, Q. Jia, J.B. Goodenough, Mastering the interface for advanced all-solid-state lithium rechargeable batteries, Proc. Natl. Acad. Sci. Unit. States Am. 113 (2016) 13313–13317.
[57] S.S. Zhang, A review on electrolyte additives for lithium-ion batteries, J. Power Sources 162 (2006) 1379–1394.
[58] J.H. Song, J.T. Yeon, J.Y. Jang, J.-G. Han, S.-M. Lee, N.-S. Choi, Effect of fluoroethylene carbonate on electrochemical performances of lithium electrodes and lithium-sulfur batteries, J. Electrochem. Soc. 160 (2013) A873–A881.
[59] X.-Q. Zhang, X.-B. Cheng, C. Xiang, Y. Chong, Q. Zhang, Fluoroethylene carbonate additives to render uniform Li deposits in lithium metal batteries, Adv. Funct. Mater. 27 (2017), 1605989.
[60] J. Wang, W. Huang, A. Pei, Y. Li, F. Shi, X. Yu, Y. Cui, Improving cyclability of Li metal batteries at elevated temperatures and its origin revealed by cryo-electron microscopy, Nat. Energy 4 (2019) 664–670.
[61] J. Zhang, J. Zhao, L. Yue, Q. Wang, J. Chai, Z. Liu, X. Zhou, H. Li, Y. Guo, G. Cui, L. Chen, Safety-reinforced poly(propylene carbonate)-based all-solid-state polymer electrolyte for ambient-temperature solid polymer lithium batteries, Adv. Energy Mater. 5 (2015), 1501082.
[62] B. Joos, T. Vranken, W. Marchal, M. Safari, M.K. Van Bael, A.T. Hardy, Eutectogels: a new class of solid composite electrolytes for Li/Li-ion batteries, Chem. Mater. 30 (2018) 655–662.
[63] C. Ma, Y. Feng, F. Xing, L. Zhou, Y. Yang, Q. Xia, L. Zhou, L. Zhang, L. Chen, D. G. Ivey, D.R. Sadoway, W. Wei, A borate decorated anion-immobilized solid polymer electrolyte for dendrite-free, long-life Li metal batteries, J. Mater. Chem. 7 (2019) 19970–19976.
[64] Z. Lin, X. Guo, H. Yu, Amorphous modified silyl-terminated 3D polymer electrolyte for high-performance lithium metal battery, Nano Energy 41 (2017) 646–653.